

Vacancy dissociation in body-centered cubic screw dislocation cores

L.M. Hale¹ and C. A. Becker²

¹*Materials Science and Engineering Division, National Institute of Standards and Technology,
100 Bureau Drive, Gaithersburg, MD 20899*

²*Office of Data and Informatics, National Institute of Standards and Technology, 100 Bureau
Drive, Gaithersburg, MD 20899*

The interaction between screw dislocations and vacancies in body-centered cubic metals is investigated using molecular dynamics simulations. For thirteen different classical interatomic potentials, materials properties relating to vacancies, dislocations, and the interaction between the two are evaluated. The potentials include six for iron, two for molybdenum, and five for tantalum, and they are a mix of embedded atom method (EAM), modified embedded atom method (MEAM), and angular dependent potential (ADP) styles. A previously unknown behavior was identified during the interaction simulations. Out of the thirteen potentials investigated, ten predict a vacancy on the dislocation core to no longer remain as a discrete point defect, but rather to dissociate along the dislocation line. The structure of the dissociation is dependent on the potential and is characterized here. As this vacancy dissociation alters the core structure of the dislocation, it may prove to be a new mechanism for dislocation pinning and pipe diffusion.

Keywords: dislocation; bcc metal; vacancy; molecular dynamics

I. INTRODUCTION

The mechanical properties of metals are intimately tied to the nature of the dislocations within the material, and how those dislocations interact with other types of defects. In particular, point defects can alter the slip nature of dislocations resulting in softening or hardening of the material, and self-point defects (vacancies and self-interstitial atoms) allow for dislocations with edge components to climb. This interaction is coupled in the sense that the presence of dislocations also alters the diffusion of the point defects. Dislocations can serve as sinks for point defects, and diffusion along dislocation lines is different than in the bulk material (pipe diffusion) [1].

Despite the importance of defect interactions, experimental measurements of behaviors and mechanisms at the relevant scales are limited. Computational tools and models can thus provide insight not easily obtained experimentally. Atomic scale calculations have been used for decades to investigate the structures, motions and interactions of point defects and dislocations. Multiple studies have performed molecular statics calculations of the vacancy formation energy near the dislocation core [2-11]. Maps of the formation energy versus position have been compared to elasticity models [2, 5], used to estimate a vacancy trap energy and radius [5, 10], and used as the foundation for modeling the vacancy diffusion pathway in and around the dislocation core using a variety of techniques [7, 9, 10, 12, 13]. A hybrid quantum-classical investigation revealed that the core reconstruction influences the interaction energy close to the dislocation core [11]. Density functional theory (DFT) calculations of impurity interstitials in body-centered cubic (bcc) iron revealed that the impurities alter the stable screw dislocation core [14].

The power of classical atomistic simulations is that they allow for the prediction of materials properties and behaviors that require both an atomistic description as well as length and time scales far beyond what can be achieved with quantum-based atomic calculations. The limitation is that their empirical nature means that the predictions obtained can be strongly potential-dependent, especially for behaviors that were not explicitly fit to. This is particularly relevant for the investigation here as, while most metallic potentials are fit with vacancy properties in mind, only a few so far have explicitly considered dislocation behaviors, and none have been fit to produce specific dislocation-vacancy interactions. Because of this, it is necessary to consider the predictions of multiple potentials, and to show how each of those potentials predicts not only the dislocation-vacancy interaction, but also the more basic properties of the isolated defects.

In this paper, we investigate the interaction of the bcc screw dislocation with vacancies using thirteen different classical interatomic potentials. The basic formation energies and structures for the isolated defects are calculated and compared. Static dislocation-vacancy interaction maps are computed showing the strength of the dislocation-vacancy interaction as a function of the radial vector from the dislocation core to the vacancy’s position. In investigating the size-dependence of the dislocation-vacancy interaction energies on the periodic z-dimension, it was revealed that a number of potentials predict the vacancy to dissociate along the dislocation line. This dissociation is characterized for all of the potentials.

II. CALCULATION METHODS

In order to differentiate the various interatomic potentials used here, we follow the convention used on the National Institute of Standards and Technology’s Interatomic Potential Repository website. The name for each potential is composed by combining the publication year, first author’s last name and initials, and short description of the model. The six potentials of iron used are 1997--Ackland-G-J--Fe [15], 2003--Mendelev-M-I--Fe-2 [16], 2003--Mendelev-M-I--Fe-5 [16], 2004--Zhou-X-W--Fe [17], 2006--Chamati-H--2006--Fe [18], and 2012--Proville-L--Fe [19]. The two potentials of molybdenum used are 2004--Zhou-X-W--Mo [17] and 2012--Park-H--Mo [20]. And, the five potentials of tantalum used are 2003--Li-Y-H--Ta [21], 2004--Zhou-X-W--Ta [17], 2013--Ravelo-R--Ta-1 [22], 2013--Ravelo-R--Ta-2 [22], and 2015--Purja-Pun-G-P--Ta [23]. All of these potentials are embedded atom method (EAM) potentials [24] with the exception of 2012--Park-H--Mo being a modified embedded atom method (MEAM) potential [25] and 2015--Purja-Pun-G-P--Ta being an angular dependent (ADP) potential [26].

Performing the calculations in a high-throughput manner was further supported by the iprPy Python-based framework (source code available at <https://github.com/usnistgov/iprPy>). This framework was developed as part of the NIST Interatomic Potential Repository project to assist in evaluating and comparing how different interatomic potentials predict a variety of basic materials properties. The atomman Python package (source code available at <https://github.com/usnistgov/atomman>) was used as a wrapper for the LAMMPS molecular dynamics software [27, 28] by preparing atomic systems, constructing LAMMPS input scripts, executing LAMMPS, and performing post-run analysis of the simulation results. Embedding the simulations in Python is advantageous as it creates a complete record of the calculation process which supports sharing the calculation code for verification and knowledge transfer.

Additionally, atomman treats LAMMPS potentials as modular entries making it easier to perform the same simulations with multiple potentials.

Lattice and elastic constants were calculated using the refine_structure calculation in iprPy. This routine starts with an initial guess for the lattice constants of a structure. System-wide pressures are evaluated statically using LAMMPS for both the initial system as well as for small strains (1×10^{-5}). The elastic constants of the system are obtained by comparing changes in stress (pressure) to changes in strain, and a new lattice parameter guess is obtained by assuming linear elasticity and extrapolating to the lattice dimensions associated with zero pressure. The calculation then iterates until the lattice parameters converge.

The iprPy calculation point_defect_static was used to compute the vacancy formation energy. Perfect systems are constructed using the refined lattice constant values, then an atom is deleted and the local atomic positions are allowed to relax to a force tolerance of 1×10^{-8} eV/Å. The formation energy is obtained as the change in energy of the system with the addition of the vacancy minus the per-atom cohesive energy of the perfect system. This is repeated for supercells ranging from $3 \times 3 \times 3$ to $10 \times 10 \times 10$, and final values are obtained by plotting the formation energy versus the inverse number of atoms and extrapolating to infinite atoms. Dislocations were investigated using dislocation monopole systems. Initially, a perfect bcc block of atoms was constructed with Cartesian axes corresponding to the crystallographic axes of $[\bar{1}2\bar{1}], [\bar{1}01], [111]$. The dimensions of the atomic block are $48a\sqrt{6} \times 80a\sqrt{2} \times Z$, where a is the cubic lattice constant and Z varies with different simulations. Z is always a multiple of $2b$, where b is the magnitude of the $a/2[111]$ Burgers vector.

A dislocation parallel to the z-axis was created by adding to the atom positions the displacements associated with the Eshelby anisotropic elasticity solution [29] for a perfectly straight dislocation. The anisotropic elasticity solution was obtained using the Stroh method [30-32] code contained in atomman.

The system is divided into two regions: an active region defined by the volume within a cylinder parallel to the z-axis, and a non-active region defined as the remaining volume of the system. The atoms in the non-active region remain fixed at the positions associated with the anisotropic displacement solution while the atoms in the active region are relaxed using energy minimization. The radius of the active region is defined such that the non-active region is always at least $3a$ thick, i.e. $r_{active} = a(20\sqrt{2} - 3) \approx 25.284a$. The atoms in the active region were relaxed by performing 10000 Nose-Hoover NVT integrations at 100 K, followed by 1000 NVT integrations with the temperature linearly scaling down to 0.01 K, and finally performing a minimization to a force tolerance of 1×10^{-5} eV/Å.

The Peierls barrier was evaluated using nudged elastic band (NEB) calculations [33, 34]. Two dislocation monopole systems with Z thickness of $2b$ are constructed in which the dislocations are one periodic distance apart along the $(\bar{1}01)$ slip plane. The NEB calculation identifies the low energy transition pathway between the two initial end states giving the non-kinked slip barrier of the dislocation.

The interaction of the dislocation with a vacancy was examined by performing multiple simulations where a single atom at radial position, \mathbf{r} , from the dislocation core's xy position was removed from the relaxed dislocation monopole system, and the system was relaxed to a force tolerance of 1×10^{-5} eV/Å. The formation energy of the vacancy near the dislocation core, $E_f(\mathbf{r})$, was then obtained by comparing the energy of the dislocation system before and after the

vacancy was added. Finally, the dislocation-vacancy interaction (DVI) energy, E_{DVI} , is taken to be the vacancy formation energy relative to the bulk formation energy, E_f^0 ,

$$E_{DVI}(\mathbf{r}) = E_f(\mathbf{r}) - E_f^0. \quad (1)$$

III. RESULTS AND DISCUSSION

A. Basic properties

The lattice constants, elastic constants, cohesive energy, vacancy formation energy, dislocation core structure and Peierls barrier shape results are summarized in Table I. These basic properties of the perfect crystal and the isolated defects of interest all influence how the defects move and interact with each other. The bulk crystal and vacancy property values can be directly compared to experimental measurements.

Across the potentials of the same element we see that the bulk property values tend to be similar, with most differences due to the potentials fitting these values precisely to different reference values. The only unexplained outlier is that the lattice constant for the 2012--Provill-L--Fe potential is noticeably smaller than the other iron potentials. There is more variation across the vacancy formation energies, but for the most part the values are near the experimental values. In fact, only the 2013--Ravelo-R--Ta-2 potential gives a formation energy outside the experimental range of values (experimentally, 2.8 ± 0.6 eV [35]).

While experimental observations cannot be directly made for the dislocation character, specific features of interest have been identified that can be compared to density functional theory (DFT) calculations. Two types of stable core configurations (Fig. 1) are observed with classical atomistic potentials: the compact (non-dissociated) core and the polarized (dissociated) core. The core structure affects kink nucleation, which in turn affects the critical resolved shear stress for slip activation, and slip direction [36]. DFT calculations of dislocation cores have revealed that for pure, perfect bcc screw dislocations at 0 K and zero stress, the stable dislocation core is compact [37-40].

The simulation results here reveal that nine out of the thirteen potentials investigated predict a compact core. During tests, it was revealed that thermally relaxing the dislocations is necessary to correctly capture the stable core structure. The elasticity solution constructs the dislocations as being compact, and only performing a minimization relaxation may not capture that the potential predicts a polarized core instead.

A second feature that affects the slip nature of the dislocation is the shape of the Peierls barrier. For potentials that predict the stable compact core, the energy pathway for slip may either be single- or double-peaked. Double-peaked Peierls barriers result from the presence of an intermediate metastable core structure. and cause partial kinks to form during slip [41], and may alter the resulting slip plane from being $\{110\}$ to being $\{112\}$ [42]. DFT calculations for all bcc transition metals reveal single-peaked Peierls barriers [39, 43-45], and low-temperature experiments show that $\{110\}$ slip is the fundamental slip plane for bcc metals [46]. The Peierls barriers for the polarized core potentials are not included here as the barrier depends on the orientation of the dislocation's polarization in the two reference states, and that the resulting slip typically involves multiple barriers along multiple $\{110\}$ planes.

Out of the nine potentials that have stable compact dislocation cores, only three show single-peaked Peierls barriers. The 2012--Provile-L--Fe potential was specifically fit to reproduce the DFT Peierls barrier, whereas the other two potentials, 2006--Chamati-H--Fe and 2012--Park-H--Mo, were not fit to this behavior specifically. Analysis of slip using the 2006--Chamati-H--Fe and 2012--Provile-L--Fe potentials reveals that the correct $\{110\}$ slip is observed when the Peierls barrier is single peaked, and the dislocation core remains compact and non-planar [47]. This is important for any investigations into the dislocation's slip behavior.

B. Dislocation-vacancy interactions

A size-dependent analysis was performed with the 2006--Chamati-H--Fe and 2012--Park-H--Mo potentials to investigate the influence of the periodic z-direction thickness, Z , on the interaction energy. With a periodic boundary, the vacancy added to the system is not actually an isolated point defect but rather an infinitely long chain of vacancies. Z ranging from $4b$ to $80b$ were explored for both dislocation-free and dislocation-containing systems to determine what thickness is necessary for the bulk vacancy formation energy, E_f^0 , and the vacancy formation energy near the dislocation, $E_f(\mathbf{r})$, to converge.

Plots of E_f^0 and $E_f(\mathbf{r})$ as a function of Z are shown in Fig. 2 for the 2006--Chamati-H--Fe potential. Values of E_f^0 and $E_f(\mathbf{r})$ with $|\mathbf{r}| > 5 \text{ \AA}$ converge within 0.0002 eV for $Z \geq 12b$. For the four unique vacancy positions with $|\mathbf{r}| < 5 \text{ \AA}$, the thickness needed to reach the same convergence increases with decreasing $|\mathbf{r}|$. Positions with $|\mathbf{r}| = 4.92 \text{ \AA}$ converge at $Z = 20b$, while positions at $|\mathbf{r}| = 3.54 \text{ \AA}$ and 2.76 \AA converge at $Z = 28b$. For the center of the core ($|\mathbf{r}| = 1.35 \text{ \AA}$), there is still an energy difference of 0.002 eV between systems of $Z = 52b$ and $Z = 56b$. In contrast, results with the Park-H--2012--Mo potential do not reveal this strong size dependence as the formation energies for all \mathbf{r} are nearly constant for $Z \geq 12b$.

Figure 3 shows the static dislocation-vacancy energy maps for all of the potentials computed using $Z = 20b$. The interaction energies are shown for vacancy positions $|\mathbf{r}| < 50 \text{ \AA}$ for all potentials. Only the qualitative appearance of the long-range interactions is considered here as these maps are very sensitive to the choice of potential. The color value range was chosen to reveal the features of the long-distance interaction. While values for small $|\mathbf{r}|$ may depend on the Z thickness, the effect is not relevant to these maps as the attractive energy at the dislocation core always greatly exceeds the plotted color value range.

There is a clear correlation between the energy maps and the character of the stable dislocation core. For nearly all of the potentials that predict the compact core to be stable, the energy map has a three-fold rotational symmetry and mirror symmetry revealing an angular dependence where long-range attraction and repulsion alternates. This is consistent with previous reports using the 2003--Mendelev-M-I--Fe-2 potential [5]. The only exception is the 2012--Provile-L--Fe potential which shows a slightly unfavorable shell region around the core, and considerably smaller long-range interaction energies than the other iron potentials.

While the compact core is believed to be the correct stable core, it is still of interest to show the interaction energy maps for polarized cores. With the 1997--Ackland-G-J--Fe, 2013--Ravelo-R--Ta-1, and 2013--Ravelo-R--Ta-2 potentials, the interaction energy maps are very similar to those observed with the compact dislocation core, except that the mirror symmetry is broken with an off-axis twist. Finally, the 2004--Zhou-X-W--Mo is unique in that the interaction energy is always attractive and depends on $|\mathbf{r}|$ without any angular dependence.

C. Vacancy dissociation

The dislocation core structure was examined more closely in order to gain insight into the strong size-dependency seen with the 2006--Chamati-H--Fe potential. In Fig. 4, the three $[111]$ columns of atoms at the center of the dislocation core are extracted and shown from the side for a $Z = 32b$ system. Figure 4(a) shows the initial unrelaxed structure, where the vacancy is clearly visible near the center of the middle (green) column of atoms. Guidelines are drawn in to show the z-position alignment of the three columns is consistent for the whole extracted section. Figure 4(b) shows the system after it has relaxed. There is no clear position for the vacancy anymore and the columns of atoms no longer line up with the guidelines. This indicates that the vacancy relaxes from a discrete position to being dissociated along the dislocation line. For bcc metals, the $[111]$ direction is a close packed direction meaning that this dissociation is similar to what is seen with a crowdion interstitial, except there is a missing atom instead of an extra one.

Simulations were performed in order to determine which potentials predict this dissociation, and to better characterize the structure of the dislocation core with the vacancy. Dislocation monopole systems with $Z = 64b$ were constructed for all of the potentials with a vacancy placed at the dislocation core. These simulations were performed in exactly the same manner as reported before, except that the thermal anneal occurred after the vacancy was inserted as opposed to before. This was done since the vacancy-free dislocation may move during a thermal anneal, and to help relax the dislocation-vacancy structure.

The atomic structure of the vacancy dissociation is explored by determining the fraction of the vacancy that is associated with each pair of atoms along the $[111]$ column of atoms containing the vacancy. Cumulatively summing this vacancy fraction along the column provides an informative method for mapping out the vacancy's position and dissociation

$$\zeta(N) = \sum_{i=1}^N \left(\frac{z^{(i)} - z^{(i-1)}}{b} - 1 \right). \quad (2)$$

Here, $z^{(i)}$ refers to the z-coordinate of the i^{th} atom in the column. The difference in z positions is scaled by b as it is the ideal z-distance between two atoms in the $[111]$ column when there is no vacancy present. The value of N can range $1 \leq N \leq B-1$, where $B = Z/b$. Note that $z^{(0)}$ is the periodic image of $z^{(B-1)}$, and that $\zeta(B-1) = 1$. Vacancies with discrete positions will show up as a sudden jump in ζ from 0 to 1, whereas fully dissociated vacancies will have ζ linearly increase from 0 to 1 over the entire periodic length.

Plots of $\zeta(N)$ vs. N for all of potentials are shown in Fig. 5 revealing a variety of vacancy dissociation behaviors. Out of all of the potentials, only three (1997--Ackland-G-J--Fe, 2012--Park-H--Mo and 2003--Li-Y-H--Ta) show a true discrete vacancy structure with a single sharp change in $\zeta(N)$ and only a slight relaxation of the atoms near the vacancy. Sharp jumps are also seen for the 2004--Zhou-X-W--Mo, except that there are two jumps indicating that the effect of the vacancy has split.

All the rest of the potentials show that the vacancy dissociates over a range of the dislocation line. For the 2003--Mendelev-M-I--Fe-2, 2003--Mendelev-M-I--Fe-5, 2004--Zhou-X-W--Fe, 2012--Proville-L--Fe, and 2004--Zhou-X-W--Ta potentials there seems to be a width for the dissociation. In contrast, the dissociation seen for the 2006--Chamati-H--Fe, 2013--

Ravelo-R--Ta-1, and 2013--Ravelo-R--Ta-2 potentials is complete across the width of the system indicating that if these potentials do have a vacancy dissociation width that it is greater than the $64b$ thickness of the system. Finally, the 2015--Purja-Pun-G-P--Ta potential appears to consist of three steps with each having roughly the same width.

No clear correlation is found between the basic properties computed here and whether a particular potential predicts a dissociated vacancy. The only possible trend is that the two molybdenum potentials predict discrete dislocation points. More examinations are needed to determine if the dissociation relates to an inherent aspect of the potential or a basic material property.

The vacancy dissociation observed with many of the potentials will likely have an effect on predicted yield and diffusion behaviors. Related to diffusion, the dissociation could prove to be a new mechanism for pipe diffusion. As the dissociation is similar to a crowdion interstitial, it is expected that the mobility barrier for vacancy diffusion along the column of atoms in which it has spread is considerably smaller than the bulk mobility barrier. Evidence for this is observed in Fig. 5 where the center of the vacancy has shifted along the z -axis for the potentials that predict the vacancy to dissociate. For example, with the 2003--Mendelev-MI--Fe-2 potential the vacancy's initial position was halfway between atoms with indices 32 and 33. After relaxation, the dissociation width crosses the periodic boundary and the center of the dissociation width is near atom index 57 indicating that the vacancy has moved roughly $25b$ along the dislocation line.

By dissociating, the vacancy may also show substantial effects on dislocation slip. The dissociated vacancy alters the dislocation's core structure over a length of the dislocation line, which will likely influence kink formation. A strong pinning effect of the dislocation is also expected due to the large formation energy of the vacancy on the dislocation core and the fact that the vacancy must revert to a discrete state in order for it to separate from the dislocation. Also, the vacancy breaks the three-fold rotational symmetry of the dislocation core, which will influence the stress-state dependent critical resolved shear stress.

The different interatomic potentials selected here reveal a wide range of predicted behaviors. This suggests more work should be done to understand what the most physically realistic behavior is, and to elucidate how the different atomistic predictions influence dynamic processes. Only then will it be known which potentials are most suited for these types of studies and what implications the behaviors will have in modeling at higher length scales.

IV. SUMMARY

The static interaction between a vacancy and a bcc screw dislocation was examined using classical atomistics and a variety of interatomic potentials. A number of basic properties related to dislocation and vacancy formation are calculated in order to characterize and compare the different potentials. All of the potentials provide decent predictions of bulk and vacancy properties. However, the dislocation core structures and Peierls barrier shapes vary due to the fact that most were not fit with these behaviors in mind.

Dislocation-vacancy interaction maps are constructed for all of the potentials. While most reveal similar qualitative behaviors, differences are observed due to how the potentials predict the relaxed dislocation core structure.

With vacancies positioned directly on the dislocation cores, an interesting new mechanism is observed in which the vacancy dissociates along the dislocation line. This vacancy dissociation is observed for many but not all of the potentials. Characterization of the

dissociation across the different potentials reveals differences in the structure of this relaxation. Further exploratory work is needed of this mechanism as it may influence dislocation pinning, vacancy trapping, and pipe diffusion.

- [1] Y. Shima, Y. Ishikawa, H. Nitta, Y. Yamazaki, K. Mimura, M. Isshiki, Y. Iijima, Self-diffusion along dislocations in ultra high purity iron, *Mater Trans* 43(2) (2002) 173-177.
- [2] E. Clouet, The vacancy-edge dislocation interaction in fcc metals: A comparison between atomic simulations and elasticity theory, *Acta Materialia* 54(13) (2006) 3543-3552.
- [3] E. Clouet, S. Garruchet, H. Nguyen, M. Perez, C.S. Becquart, Dislocation interaction with C in α -Fe: A comparison between atomic simulations and elasticity theory, *Acta Materialia* 56(14) (2008) 3450-3460.
- [4] E. Clouet, L. Ventelon, F. Willaime, Dislocation core energies and core fields from first principles, *Phys Rev Lett* 102(5) (2009) 055502.
- [5] E. Hayward, C. Deo, B.P. Uberuaga, C.N. Tome, The interaction of a screw dislocation with point defects in bcc iron, *Philosophical Magazine* 92(22) (2012) 2759-2778.
- [6] K.M. Miller, Point Defect-Dislocation Interactions in Molybdenum, *J Phys F Met Phys* 11(6) (1981) 1175-1189.
- [7] K.M. Miller, K.W. Ingle, A.G. Crocker, A Computer-Simulation Study of Pipe Diffusion in Body-Centered Cubic Metals, *Acta Metall Mater* 29(9) (1981) 1599-1606.
- [8] V. Shastri, T.D. de la Rubia, The interaction between point defects and edge dislocation in BCC iron, *Journal of Engineering Materials and Technology-Transactions of the Asme* 121(2) (1999) 126-128.
- [9] A.B. Sivak, V.M. Chernov, V.A. Romanov, P.A. Sivak, Kinetic Monte-Carlo simulation of self-point defect diffusion in dislocation elastic fields in bcc iron and vanadium, *J Nucl Mater* 417(1-3) (2011) 1067-1070.
- [10] A.B. Sivak, V.A. Romanov, V.M. Chernov, Diffusion of Self-Point Defects in Body-Centered Cubic Iron Crystal Containing Dislocations, *Crystallogr Rep* 55(1) (2010) 97-108.
- [11] F. Tavazza, R. Wagner, A.M. Chaka, L.E. Levine, Vacancy formation energy near an edge dislocation: A hybrid quantum-classical study, *Materials Science and Engineering: A* 400-401 (2005) 72-75.
- [12] R.C. Picu, D. Zhang, Atomistic study of pipe diffusion in Al-Mg alloys, *Acta Materialia* 52(1) (2004) 161-171.
- [13] Q.F. Fang, R. Wang, Atomistic simulation of the atomic structure and diffusion within the core region of an edge dislocation in aluminum, *Physical Review B* 62(14) (2000) 9317-9324.
- [14] L. Ventelon, B.L. Uethi, E. Clouet, L. Proville, B. Legrand, D. Rodney, F. Willaime, Dislocation core reconstruction induced by carbon segregation in bcc iron, *Physical Review B* 91(22) (2015).
- [15] G.J. Ackland, D.J. Bacon, A.F. Calder, T. Harry, Computer simulation of point defect properties in dilute Fe-Cu alloy using a many-body interatomic potential, *Philos Mag A* 75(3) (1997) 713-732.
- [16] M.I. Mendelev, S. Han, D.J. Srolovitz, G.J. Ackland, D.Y. Sun, M. Asta, Development of new interatomic potentials appropriate for crystalline and liquid iron, *Philosophical Magazine* 83(35) (2003) 3977-3994.
- [17] X.W. Zhou, R.A. Johnson, H.N.G. Wadley, Misfit-energy-increasing dislocations in vapor-deposited CoFe/NiFe multilayers, *Physical Review B* 69(14) (2004).

- [18] H. Chamati, N.I. Papanicolaou, Y. Mishin, D.A. Papaconstantopoulos, Embedded-atom potential for Fe and its application to self-diffusion on Fe(100), *Surf Sci* 600(9) (2006) 1793-1803.
- [19] L. Proville, D. Rodney, M.C. Marinica, Quantum effect on thermally activated glide of dislocations, *Nat Mater* 11(10) (2012) 845-9.
- [20] H. Park, M.R. Feller, T.J. Lenosky, W.W. Tipton, D.R. Trinkle, S.P. Rudin, C. Woodward, J.W. Wilkins, R.G. Hennig, Ab initio based empirical potential used to study the mechanical properties of molybdenum, *Physical Review B* 85(21) (2012).
- [21] Y.H. Li, D.J. Siegel, J.B. Adams, X.Y. Liu, Embedded-atom-method tantalum potential developed by the force-matching method, *Physical Review B* 67(12) (2003).
- [22] R. Ravelo, T.C. Germann, O. Guerrero, Q. An, B.L. Holian, Shock-induced plasticity in tantalum single crystals: Interatomic potentials and large-scale molecular-dynamics simulations, *Physical Review B* 88(13) (2013).
- [23] G.P. Purja Pun, K.A. Darling, L.J. Kecskes, Y. Mishin, Angular-dependent interatomic potential for the Cu-Ta system and its application to structural stability of nano-crystalline alloys, *Acta Materialia* 100 (2015) 377-391.
- [24] M.S. Daw, M.I. Baskes, Embedded-Atom Method - Derivation and Application to Impurities, Surfaces, and Other Defects in Metals, *Physical Review B* 29(12) (1984) 6443-6453.
- [25] M.I. Baskes, Modified embedded-atom potentials for cubic materials and impurities, *Phys Rev B Condens Matter* 46(5) (1992) 2727-2742.
- [26] Y. Mishin, M.J. Mehl, D.A. Papaconstantopoulos, Phase stability in the Fe-Ni system: Investigation by first-principles calculations and atomistic simulations, *Acta Materialia* 53(15) (2005) 4029-4041.
- [27] S. Plimpton, Fast Parallel Algorithms for Short-Range Molecular-Dynamics, *J Comput Phys* 117(1) (1995) 1-19.
- [28] <http://lammps.sandia.gov>.
- [29] J.D. Eshelby, W.T. Read, W. Shockley, Anisotropic Elasticity with Applications to Dislocation Theory, *Acta Metall Mater* 1(3) (1953) 251-259.
- [30] A.N. Stroh, Steady State Problems in Anisotropic Elasticity, *J Math Phys Camb* 41(2) (1962) 77-&.
- [31] A.N. Stroh, Dislocations and Cracks in Anisotropic Elasticity, *Philosophical Magazine* 3(30) (1958) 625-&.
- [32] J.P. Hirth, J. Lothe, Theory of dislocations, 2nd ed., Krieger Pub. Co., Malabar, FL, 1992.
- [33] G. Henkelman, H. Jonsson, Improved tangent estimate in the nudged elastic band method for finding minimum energy paths and saddle points, *J Chem Phys* 113(22) (2000) 9978-9985.
- [34] G. Henkelman, B.P. Uberuaga, H. Jonsson, A climbing image nudged elastic band method for finding saddle points and minimum energy paths, *J Chem Phys* 113(22) (2000) 9901-9904.
- [35] K. Maier, M. Peo, B. Saile, H.E. Schaefer, A. Seeger, High-temperature positron annihilation and vacancy formation in refractory metals, *Philosophical Magazine A* 40(5) (1979) 701-728.
- [36] G.F. Wang, A. Strachan, T. Cagin, W.A. Goddard, Kinks in the $a/2 < 111 >$ screw dislocation in Ta, *Journal of Computer-Aided Materials Design* 8(2-3) (2002) 117-125.
- [37] S.L. Frederiksen, K.W. Jacobsen, Density functional theory studies of screw dislocation core structures in bcc metals, *Philosophical Magazine* 83(3) (2003) 365-375.
- [38] S. Ismail-Beigi, T.A. Arias, Ab initio study of screw dislocations in Mo and Ta: A new picture of plasticity in bcc transition metals, *Physical Review Letters* 84(7) (2000) 1499-1502.

- [39] L. Ventelon, F. Willaime, Core structure and Peierls potential of screw dislocations in α -Fe from first principles: cluster versus dipole approaches, *Journal of Computer-Aided Materials Design* 14 (2007) 85-94.
- [40] C. Woodward, S.I. Rao, Flexible ab initio boundary conditions: Simulating isolated dislocations in bcc Mo and Ta, *Physical Review Letters* 88(21) (2002) 216402.
- [41] P.A. Gordon, T. Neeraj, Y. Li, J. Li, Screw dislocation mobility in BCC metals: the role of the compact core on double-kink nucleation, *Model Simul Mater Sc* 18(8) (2010) 085008.
- [42] L.M. Hale, J.A. Zimmerman, C.R. Weinberger, Simulations of bcc tantalum screw dislocations: Why classical inter-atomic potentials predict $\{112\}$ slip, *Computational Materials Science* 90 (2014) 106-115.
- [43] D.E. Segall, A. Strachan, W.A. Goddard, S. Ismail-Beigi, T.A. Arias, Ab initio and finite-temperature molecular dynamics studies of lattice resistance in tantalum, *Physical Review B* 68(1) (2003) 014104.
- [44] L. Ventelon, F. Willaime, E. Clouet, D. Rodney, Ab initio investigation of the Peierls potential of screw dislocations in bcc Fe and W, *Acta Materialia* 61(11) (2013) 3973-3985.
- [45] C.R. Weinberger, G.J. Tucker, S.M. Foiles, Peierls potential of screw dislocations in bcc transition metals: Predictions from density functional theory, *Physical Review B* 87(5) (2013).
- [46] C.R. Weinberger, B.L. Boyce, C.C. Battaile, Slip planes in bcc transition metals, *International Materials Reviews* 58(5) (2013) 296-314.
- [47] L.M. Hale, H. Lim, J.A. Zimmerman, C.C. Battaile, C.R. Weinberger, Insights on activation enthalpy for non-Schmid slip in body-centered cubic metals, *Scripta Mater* 99 (2015) 89-92.

TABLE I. List of the potential models investigated and basic properties for each. The lattice constant, a_0 , is in Å, the elastic constants, C_{ij} , are in GPa, and the cohesive energy, E_{coh} , and bulk vacancy formation energy, E_f^0 , are in eV.

Potential	Style	a_0	E_{coh}	C_{11}	C_{12}	C_{44}	E_f^0	dislocation core	Peierls shape
1997--Ackland-G-J--Fe	EAM	2.8665	-4.32	243.4	145.1	116.0	1.70	Polarized	
2003--Mendeleev-M-I--Fe-2	EAM	2.8553	-4.12	243.4	145.0	116.0	1.71	Compact	Double
2003--Mendeleev-M-I--Fe-5	EAM	2.8553	-4.13	243.9	145.3	116.1	1.63	Compact	Double
2004--Zhou-X-W--Fe	EAM	2.8659	-4.29	231.3	136.7	117.8	1.67	Compact	Double
2006--Chamati-H--Fe	EAM	2.8665	-4.28	241.1	146.8	114.0	1.86	Compact	Single
2012--Proville-L--Fe	EAM	2.8148	-4.12	243.4	145.0	116.0	1.96	Compact	Single
2004--Zhou-X-W--Mo	EAM	3.1502	-6.81	456.3	167.4	115.3	2.95	Polarized	
2012--Park-H--Mo	MEAM	3.1674	-6.82	423.3	143.1	95.5	2.96	Compact	Single
2003--Li-Y-H--Ta	EAM	3.3026	-8.09	247.5	143.6	86.6	2.75	Compact	Double
2004--Zhou-X-W--Ta	EAM	3.3025	-8.09	264.4	159.5	80.9	2.98	Compact	Double
2013--Ravelo-R--Ta-1	EAM	3.3040	-8.10	262.6	160.7	81.8	2.40	Polarized	
2013--Ravelo-R--Ta-2	EAM	3.3040	-8.10	266.9	160.4	86.0	1.96	Polarized	
2015--Purja-Pun-G-P--Ta	ADP	3.3040	-8.10	268.9	157.6	90.4	3.06	Compact	Double

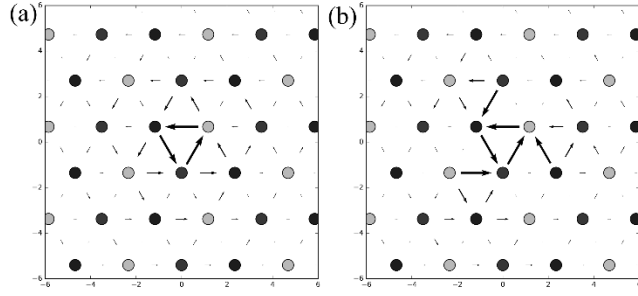


FIG. 1: Differential displacement maps of bcc screw dislocations showing (a) the compact core structure and (b) the dissociated/polarized core structure.

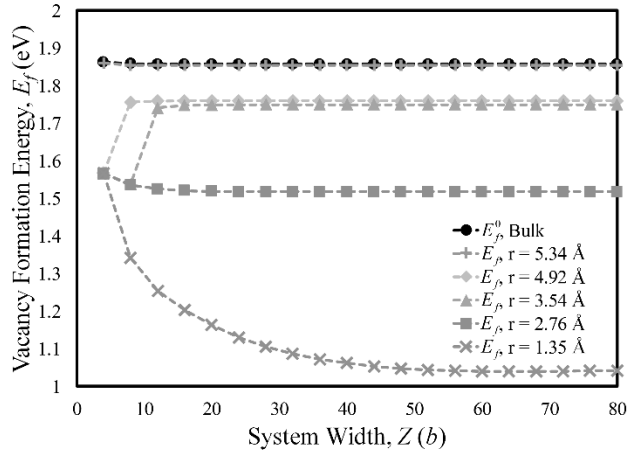


FIG. 2. Size dependent investigation of the vacancy formation energies with respect to system width using the 2006--Chamati-H--Fe potential.

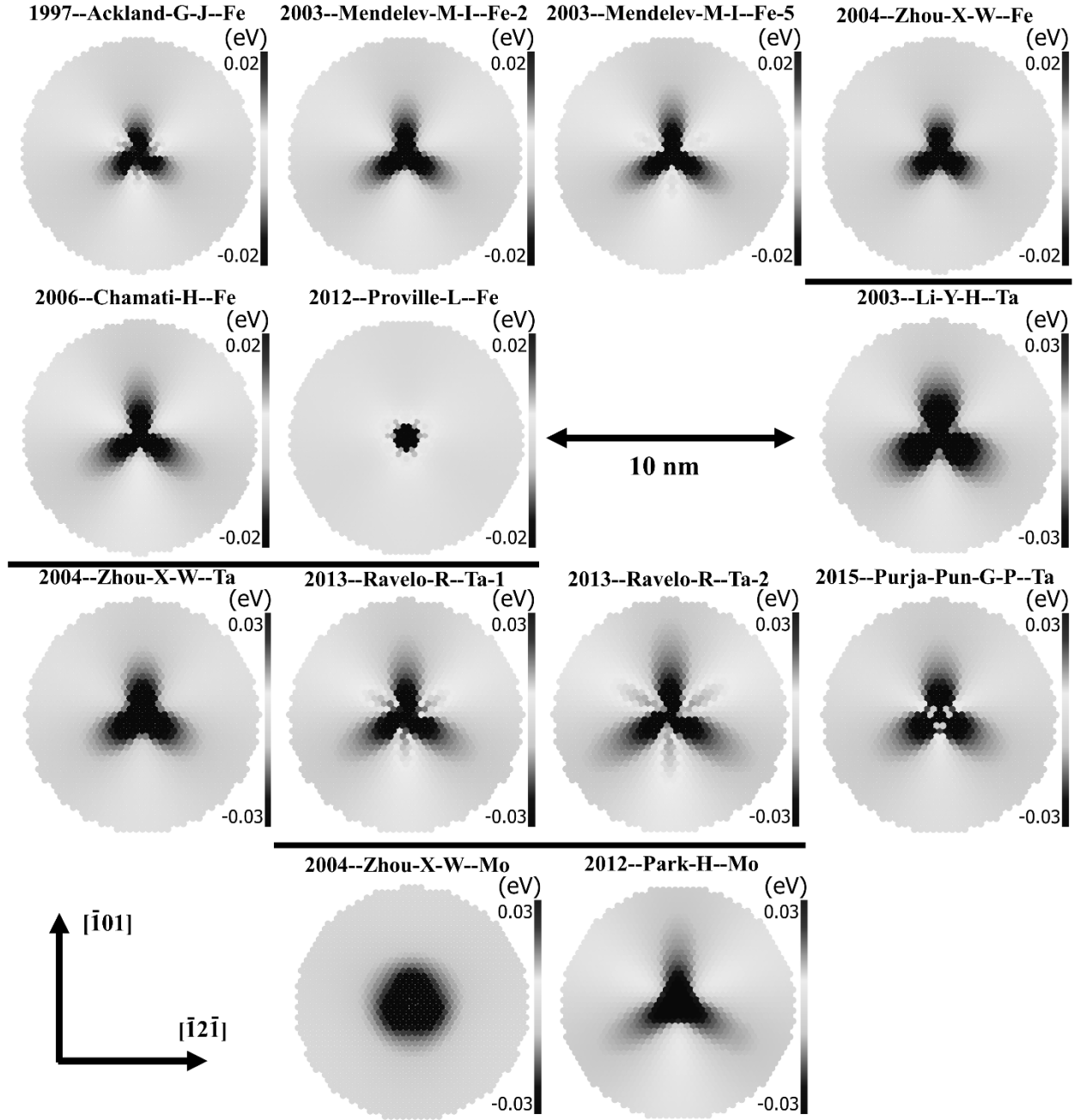


FIG. 3. Maps of the interaction energy between a screw dislocation and a vacancy at different positions relative to the dislocation core.

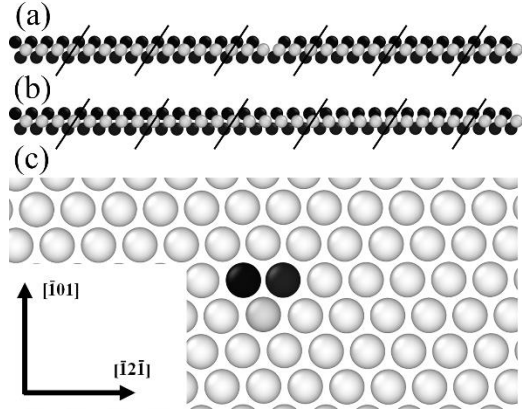


FIG. 4. Cross-section view of the three columns of atoms at the center of the dislocation core $32b$ long showing vacancy dissociation. (a) Before relaxation the vacancy is clearly visible in the center of the top (blue) column of atoms. (b) After relaxation there is no discrete vacancy position observed. The black lines are guides showing that the alignment of atoms changes from (a) to (b) indicating that the vacancy has spread along the dislocation column. (c) Top-down view indicating the three columns of atoms shown in (a) and (b).

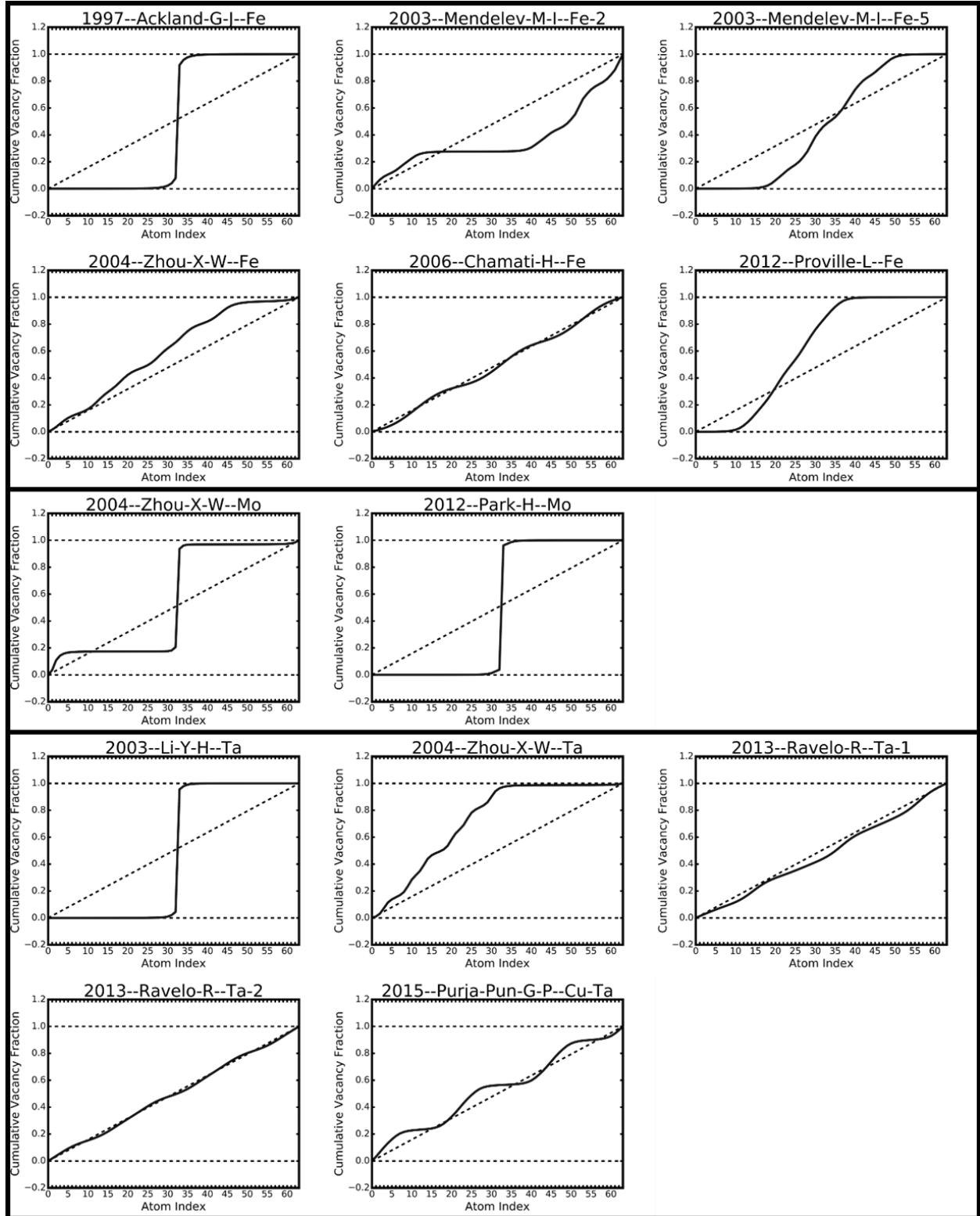


FIG. 5. Cumulative vacancy fraction plots showing the various vacancy dissociation behaviors across the different potentials.